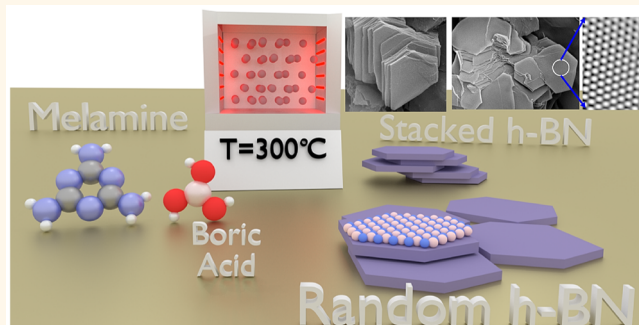


Synthesis of Low-Density, Carbon-Doped, Porous Hexagonal Boron Nitride Solids

Chandkiram Gautam,^{*,†,‡} Chandra Sekhar Tiwary,^{*,‡} Sujin Jose,^{‡,§} Gustavo Brunetto,^{‡,||} Sehmus Ozden,[‡] Soumya Vinod,[‡] Prasanth Raghavan,[‡] Santoshkumar Biradar,[‡] Douglas Soares Galvao,^{||} and Pulickel M. Ajayan^{*,‡}

[†]Department of Physics, University of Lucknow, Lucknow, India 226007, [‡]Department of Materials Science and Nano Engineering, Rice University, Houston, Texas 7005, United States, [§]School of Physics, Madurai Kamaraj University, Madurai 625021, Tamil Nadu, India, and ^{||}Department of Applied Physics, State University of Campinas, Campinas SP 13083-959, Brazil

ABSTRACT Here, we report the scalable synthesis and characterization of low-density, porous, three-dimensional (3D) solids consisting of two-dimensional (2D) hexagonal boron nitride (h-BN) sheets. The structures are synthesized using bottom-up, low-temperature (~ 300 °C), solid-state reaction of melamine and boric acid giving rise to porous and mechanically stable interconnected h-BN layers. A layered 3D structure forms due to the formation of h-BN, and significant improvements in the mechanical properties were observed over a range of temperatures, compared to graphene oxide or reduced graphene oxide foams. A theoretical model based on Density Functional Theory (DFT) is proposed for the formation of h-BN architectures. The material shows excellent, recyclable absorption capacity for oils and organic solvents.



KEYWORDS: hexagonal boron nitride nanosheets · electron microscopy · mechanical properties · oil adsorption · DFT simulations

Novel three-dimensional (3D) structures using 2D sheet-based assemblies have been synthesized by different approaches.^{1–3} Among these, the architectures made of graphene are reported to have applications in electronics, catalysis devices and sensors.^{4–6} Recently, low-density hexagonal boron nitride (h-BN) (also known as white graphene) has attracted the attention of many researchers. h-BN presents exceptional mechanical, optical and thermal properties.^{7–9} Among all the h-BN properties, its resistance against oxidation and corrosion have attracted the attention of scientific and industry communities. In recent years, several studies concerning the synthesis of h-BN nanostructures have been reported. The synthesis of nanostructures with particular morphologies as nanotubes, nanocapsules, nanocages, porous structures, and hollow spheres has been extensively studied.^{10–14} However, building interconnected 3D porous

structure using the bottom up approach remains as a challenge and has a great potential for future applications in materials science. The most common method to prepare h-BN is using high temperature synthesis (~ 1500 °C).¹⁵ In this method, the high temperature reaction consists of mixing of two compounds that are source of boron (e.g., boric acid, boron trioxide, borax) and nitrogen (e.g., ammonia, urea). However, the high temperature involved in the synthesis decreases the ability to obtain complex shapes and increase the cost of production.¹⁶ To overcome these difficulties, huge efforts were made in order to find different routes to produce h-BN at low temperature, e.g., using different reactants.¹⁷ A new synthesis route proposed by Liu *et al.*¹⁸ allows template free 3D h-BN structure using nitrogen/hydrogen atmosphere subject to temperature of 1000 °C. Utilizing similar conditions, Zhao *et al.*¹⁹ synthesized porous 3D structure without using catalysts

* Address correspondence to cst.iisc@gmail.com, gautam_ceramic@yahoo.com, ajayan@rice.edu.

Received for review August 15, 2015 and accepted November 18, 2015.

Published online November 18, 2015
10.1021/acsnano.5b05847

© 2015 American Chemical Society

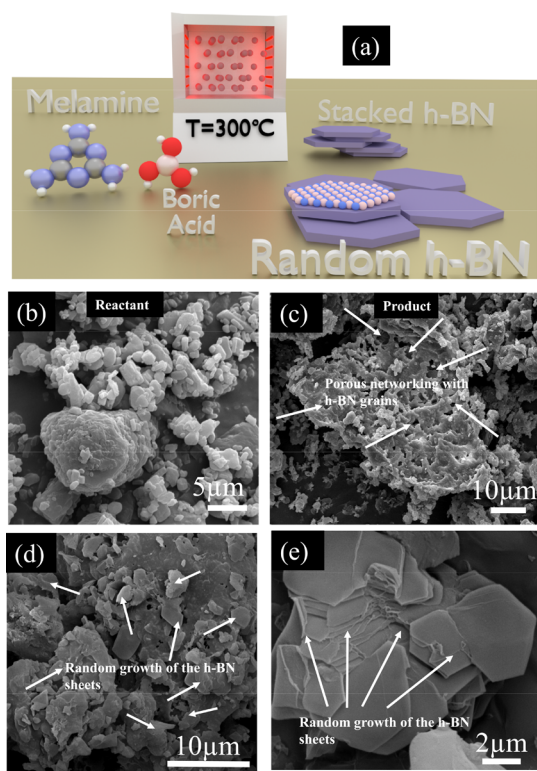


Figure 1. Surface morphology of porous BN. (a) Schematic of the proposed synthesis methodology. (b) High-magnification SEM image revealing the tiny and big sheets of boric acid and melamine sheets are aggregated to each other. (c) Low-magnification SEM image of porous h-BN sintered at 300 °C for 9 h and showing more porous well interconnected h-BN sheets within the residual glassy matrix. (d) High-magnification SEM image showed the formation of distorted h-BN sheets. (e) High-magnification SEM image showed the formation of staked h-BN sheets.

or templates. Though important advancements have been reported, the low temperature synthesis of 3D porous structure based on h-BN and having high surface area still remains a challenge.

In the present study, we report low temperature (~ 300 °C) synthesis of low-density porous 3D h-BN using a bottom up approach of the solid-state route. The synthesized structure demonstrates structural stability with low density and engineered morphology. Besides the mechanical stability, they showed good oil absorption and high resistance to corrosion under acid treatment. We carried out density functional theory (DFT) calculations on model systems to propose a growth mechanism of the synthesized nanostructures.

RESULTS AND DISCUSSION

We report the solid state synthesis of porous h-BN structure using a mixture of boric acid (H_3BO_3) and melamine ($C_3N_6H_6$). The reaction was carried out at 300 °C (shown in Figure 1a) and the obtained products were analyzed for different time intervals of 3, 6, and 9 h. X-ray powder diffraction (Figure S1 in Supporting Information) of the initial mixture and the product

revealed the formation of h-BN structures. The X-ray photoelectron spectroscopy (XPS), (Figure S2 in Supporting Information) analysis confirmed the presence of the elements B (boron) and N (nitrogen) (inset Figure S2 in Supporting Information). The peaks observed at 191.1 and 398.1 eV (inset Figure S2a in Supporting Information) could be associated, respectively, with boron and nitrogen 1s-core level and are characteristics of a h-BN bulk structure.^{20–22} Along with B and N, it was also observed that the carbon (287 eV) and oxygen (535 eV) elements were present in the porous h-BN. FTIR spectrum (Figure S3 in Supporting Information) showed peaks associated with the B–N bonds at 1400 and 779 cm⁻¹, corresponding to B–N stretching and B–N–B bending vibrations, respectively.^{23,24} The peak located at 1190 cm⁻¹ could be assigned to the B–O–H bending vibrations. The strong IR absorption peaks at 3180 cm⁻¹ could be attributed to the O–H vibrations.

In order to understand the reaction kinetics, differential thermal analysis (DTA) and thermogravimetric analysis (TGA) were performed (Figure S4 in Supporting Information). The DTA results revealed two endothermic peaks situated at different temperatures 163 and 342 °C.^{25,26} Both peaks could be assigned to those of the boric oxide and the melamine, respectively. The TG-DTA curves also indicated a weight loss occurred during the precursor evaporation. The evaporation process is responsible for the generation of porous structure and the enhancement of surface area.^{27,28}

Scanning electron microscopy (SEM) of initial powder (Figure 1b) showed a bimodal particle size consisting of the two reactants (H_3BO_3 and $C_3N_6H_6$) with random particle morphology. The processed sample (Figure 1c) showed a porous interconnected structure. More detailed images (Figure 1d,e) showed thin sheets stacked on top of each other both in horizontal and vertical directions embedded in the matrix. Energy dispersive X-ray spectroscopy (EDS) analysis showed that the hexagonal sheets were composed mostly of B and N in the matrix region of C. Detailed transmission electron microscopy (TEM) (Figure 2) images revealed the presence of layers with a thickness of less than 2 nm and the 2D sheets with large amount of porosity. Through analysis of the images, it was possible to identify porous distribution along the h-BN sheets. Energy filter composition map showed that the chemical composition of the 2D sheets was mostly made of B (Figure 2c) and N (Figure 2d). The microstructure of the porous h-BN sheet was further investigated by HRTEM (High Resolution TEM) imaging. The HRTEM image (Figure 2e) showed that the atoms were arranged in a hexagonal symmetry, with the lattice constant similar to the h-BN previously reported.^{29,30} Besides the hexagonal atomic arrangement, HRTEM image (Figure 2f) revealed a layered h-BN structure with an interlayer distance of 0.34 nm (Figure 2g)

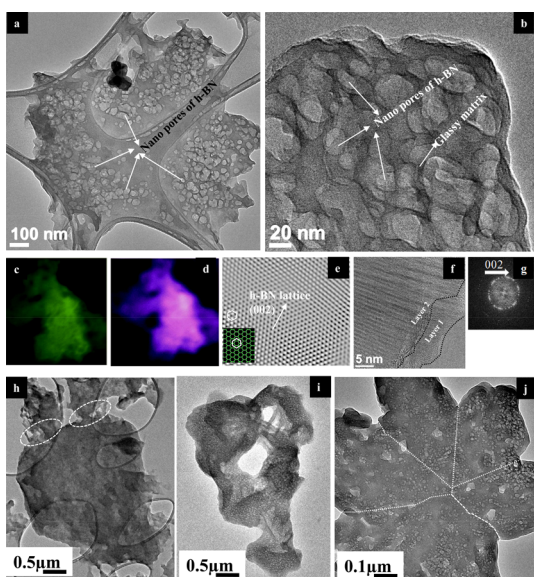


Figure 2. Nanostructures of porous h-BN. (a) Low-magnification bright field TEM image showing large h-BN sheet with porosity. (b) High-magnification bright field image showing uniform distribution of the porosity. (c and d) EELS map of B and N of the sheets. (e) HRTEM image showing hexagonal lattice. (f) High-magnification image at the edge of the sheet showing the number of layer in these large size sheets. (g) The selected area electron diffraction (SAED) patterns showing hexagonal pattern of h-BN. Bright field TEM image of (h) the sintered interface marked in white circle showing how the two h-BN sheets. (i) Interconnected h-BN sheets. (j) Several sheets welded together at the edge to give rise to a porous structure.

corresponding to the interplane distance (002). The low-magnification images (Figure 2h–j) showed interconnected adjacent layers (the dotted lines, in Figure 2h,i, highlight the connections). The final structure presented some holes with diameter ranging from 20 to 100 nm. During the synthesis procedure, the decomposition of boric acid and melamine released gases like NH_3 , N_2 and CO which created bubbles and suppressed the h-BN growths in these regions. Once the gas was released, through the natural spaces between the layers, voids were created in regions that were formerly filled with bubbles, giving rise to a porous structure.³¹ The low-magnification SEM image revealed a porous bulk network between the h-BN sheets and the residual glassy matrix of carbon and oxygen. On the other hand, high-magnification SEM micrograph showed fully developed and vertically aligned h-BN sheets, whose size varied from 1 to 4 μm (Figure S5b in Supporting Information). The pores sizes were proportional with the soaking time that was consistent with porosity and surface area measurements.

In order to understand the formation mechanism of 2D sheet along with porosity, we performed density functional theory to model the system in order to propose assembly mechanism due to the reaction between boric acid and melamine. Electrostatic

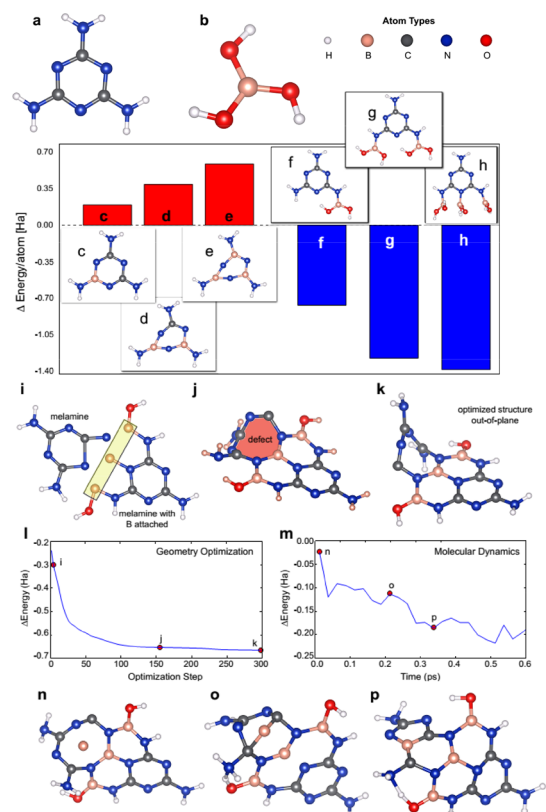


Figure 3. Geometry optimization and molecular dynamic simulations. (a) Melamine and (b) boric acid molecular structures. (c–e) Energy/atom, in relation with the pristine melamine, to systematically substitute carbon by boron atoms. (f–h) Energy/atom, in relation to the pristine melamine, to systematically add boron atoms in the edge of the melamine molecule. (i–l) Geometry optimization steps when a second melamine molecule is included to increase the size of the BCN structure. The final optimized geometry presents a structural defect and has out-of-plane conformation. (m–p) Molecular dynamics when a boron atom is *ad hoc* placed close to the defect. The time evolution shows that the introduced boron can interact with the defective site and the final structure evolves to a planar configuration and composed mostly by hexagons.

interaction between melamine (Figure 3a) and boric acid (Figure 3b) can yield two-dimensional (2D) ordered structures.³² However, the formation of BCN structures was only observed when extra energy, e.g., heat, was introduced in the system.³³ We carried out DFT calculations to propose a possible way to obtain BCN structures. Our analyses were based on structure energies comparisons and *ab initio* molecular dynamics (AIMD) simulations. We proposed two different approaches to start the formation of the BCN structures. In the first one, the structure was built by a gradual substitution of carbon by boron atoms in the melamine central ring (Figure 3c–e). The second one consisted of attachment of boron into the edges of the melamine (Figure 3f–h). In all cases, we compare the proposed structure energy with the total energy of melamine (used as reference energy). Due to the different number of atoms between the considered structures, the analyses were carried out considering

the average energy (energy/atom). In the first approach, the initial substitution $C \rightarrow N$ (Figure 3c) yielded a final structure, which was less stable than the melamine, *i.e.*, its total energy was about 0.2 Ha/atom higher. Besides the increase in the total energy, the first substitution caused the ring angles to deform and one of them decreased from 126 ($N-C-N$) to 111° ($N-B-N$). When the second boron was included, substituting another carbon atom (Figure 3d), the ring geometry became even more deformed. This substitution caused the energy of the structure to increase around 0.39 Ha/atom in relation with the melamine energy. In addition, the ring geometry became more stretched, with the two angles $N-B-N$ measuring 69 and 110°. The substitution of the last carbon caused the energy increase around 0.19 Ha/atom in comparison to the former structure (ring with 2 boron atoms).

The second approach to the formation of BCN structures was based on the attachment of boron structures to the edge of the melamine (Figure 3f–h). We substituted one of the hydrogen belonging to the melamine with a part of the boric acid molecule. The energy of the first two substitutions (Figure 3f,g) yielded structures 0.75 and 1.24 Ha/atom, more stable in comparison to the melamine molecule, and the geometry remained planar. When the third boron was inserted (Figure 3h), the energy dropped by 0.11 Ha/atom in comparison to the structure containing two boron atoms (Figure 3g). The insertion of the third boron caused rearrangement of the oxygen atoms out of the molecule plane. On the basis of energy analysis, we propose that the initial assembly of BCN structures, considering melamine as initial seed, was more favorable through the edge instead of selective substitution of carbon atoms from the initial seed (melamine). Starting with a configuration where the melamine already had three boron atoms in its edge, we went one step further in the assembly process by approximating a second melamine molecule (Figure 3i). In that case, some hydrogen and oxygen atoms were removed from the edges to ease the process. Starting from the configuration represented in Figure 3i, we carried out a geometry optimization. The relaxed geometry (Figure 3j–l) yielded a structure in which an 8-atoms ring (defect) lies in two different planes (Figure 3k).

We propose a way to fix the defect created by the addition of the second melamine in the structure. An isolated boron atom was placed close to the defective ring (Figure 3n), but far enough not to interact at the beginning. An initial velocity (10 Å/ps) was attributed to the added B atom, directed to the center of the defect ring and the whole system evolved in time. We considered an isolated atom in order to accelerate the process due to computational time limitation. We observed that, when the boron atom started to

interact with the system, the geometry of the defective ring started to change (Figure 3o) (movie M1 in Supporting Information), as well as the system energy started to decrease (Figure 3m). The system was evolved during 0.6 ps, and due to the interaction with the added atom, the 8-atoms ring was transformed into two rings with 5 and 6 atoms, respectively (Figure 3p). The obtained structure was planar and showed to be stable up to 700 °C.

After a structural characterization of the synthesized structures, we carried out mechanical tests and evaluated its performance in oil absorption. For the mechanical test, sample was subjected to compression by using Instron universal testing machine. The compressive stress–strain curves exhibited an elastic and small plastic region (Figure 4a). The measured stresses were in the range of 46.47–83.18 MPa (depending of the sample soaking time) which were higher (around 84%–91%) than previous reported values.³⁴ The samples showed an average fracture strain ranging between 11 and 15% and also depending on the sample soaking time. During the compression test, the 3D porous structures showed a remarkable deformability, as can be seen in the insets of Figure 4a. The high load bearing capacity of the 3D structure is showed in Figure 4b. SEM images of the compressed samples were taken to verify the 3D porous structure after the loading procedure. The images revealed that the h-BN sheets interlock the crack propagation. The white arrows in Figure 4c,d highlighted the h-BN sheets interlocking in the formed cracks (highlight by red circles). Low-magnification SEM image (Figure 4d) showed the distribution of h-BN sheets and how the cracked area were interlocked with them. These sheets prevented the crack propagation from one end to another, which is represented by the oval shape red color dashes (Figure 4d).

We observed that the presented bottom up approach gave rise to 3D porous and stable structures. The current synthesis protocol is suitable for designing complicated shapes by using the desired framework. We demonstrated this ability using a chicken bone as mold, as shown in Figure 4e. To obtain the 3D BCN based chicken bone, the mold was filled with the reactants and heated at 300 °C and the final product took the shape of the complicated chicken bone. Hence, the current method not only reduces energy of processing (due to the smaller needed temperature) but also gives rise to the possibility to design any desired shape. The density of the product was measured and compared with bulk density of the precursor materials (Figure 4f). The standard density of melamine, boric acid, and h-BN are 1.57, 1.44, and 2.10 g/cm³, respectively. However, the values of the densities of synthesized porous h-BN obtained for different soaking times (3, 6, and 9 h) were 0.92, 0.89, and 0.87 g/cm³, respectively. The porosity percentage becomes greater

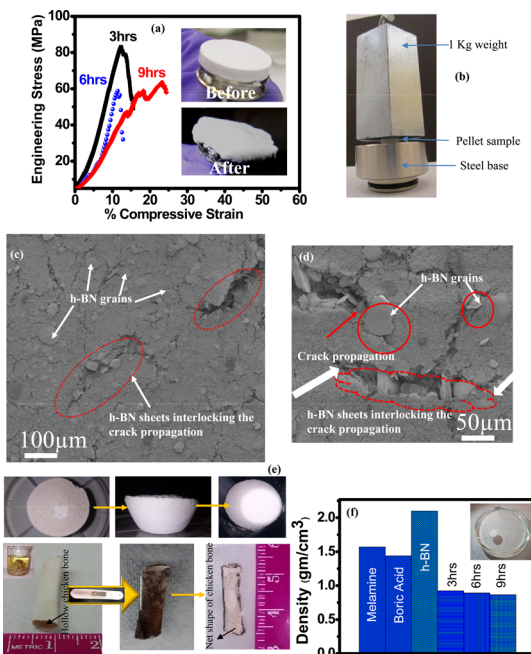


Figure 4. Mechanical characterizations of the porous h-BN. (a) Compression test results on Instron showing a linear increase in stress until $\sim 12\%$ strain and thereafter showing ductile behavior due to the formation of h-BN. The inset shows the pellet samples view before the test and after fracture test. (b) Demonstration of load bearing capacity (1 kg weight on the top of the pellet and not any damage or fracture observed which proves the high load bearing capacity of h-BN material. (c) At very low magnification, SEM image showing the crack propagation. (d) High-magnification SEM images of fractured sample revealing the h-BN sheets are interlocking the crack propagation, which is represented by white color wide arrows, located at the end of the crack propagation and large cracked propagation area covered by the red color dashes oval. (e) Net shape gain ability of the porous h-BN: initial mixture sintered in porcelain crucible at $300\text{ }^{\circ}\text{C}$ for 3 h without any external pressure and showing the net shape gain of the crucible (top view) and hollow chicken bone of diameter $\sim 5\text{ mm}$ (front view). The inset shows the cleaning of the chicken bone in the HCl solution. Hollow and cleaned chicken bone filled by the initial mixture of boric acid and melamine, kept in porcelain boat crucible, and sintered at $300\text{ }^{\circ}\text{C}$ for 3 h. Porous h-BN powder formed in net shape of the bone. (f) Density vs soaking time showing comparative density with standard density of the boric acid, melamine, h-BN and calculated after sintering for 3, 6, and 9 h. The bar graphs of density reveal that h-BN density was very low $0.867\text{ g}/\text{cm}^3$.

(55.97, 57.42, and 58.67%) with the increase of the soaking time (Figure S5a in Supporting Information). The surface area increases with increase in the soaking time (Figure S5b in Supporting Information). The values of the surface area and pore size of the synthesized carbon-doped h-BN lie in the range from 1.212 to $1.465\text{ m}^2/\text{g}$ and 1.113 to 3.168 nm , respectively.

The other important characteristic of the proposed material is the ability of removal of oils and organic contaminants from water. Materials with this property have attracted immense commercial interest, as for example, oil can be removed from water.³⁵ This characteristic that renders good absorption property to this

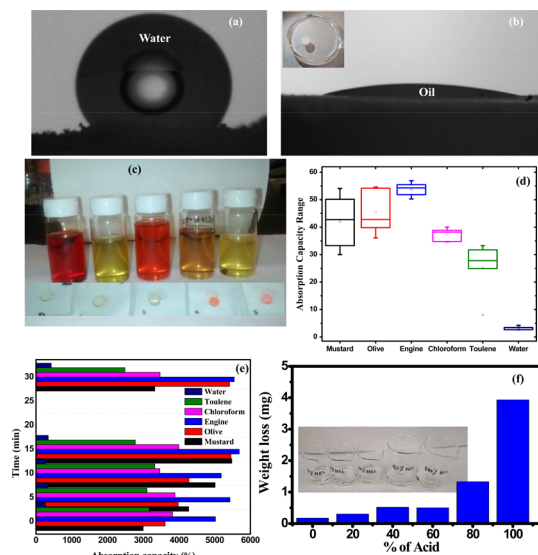


Figure 5. Oil and organic solutions absorption properties and acid corrosion resistance. (a) Contact angles measurements with DI water and showing hydrophobicity with water and (b) engine oil with h-BN sample and showing superoleophilicity. (c) Demonstration for the used oil and organic solvents along with the pellets after absorption; the red color in the oil is due to the Sudan red color dye for contrast purpose. (d and e) Absorption capacity of porous h-BN sample sintered at $300\text{ }^{\circ}\text{C}$ for 3 h soaking time for different oils and common organic solvents and showing highest oil absorption capacity for engine oil ~ 5549 for 30 min soaking time. (f) Variation of weight loss with different percentage of HCl acid for 30 min soaking time and showing the corrosion effect on synthesized porous h-BN.

material actually comes from its porous structure and high surface area. Therefore, the synthesized 3D architecture is being anticipated to find industrial applications such as water-repelling, antifouling, self-cleaning, and anticorrosion systems. It was observed that porous h-BN samples exhibited hydrophobicity (contact angle range from 58° to 134° , for different heat treated condition). On the other hand, in case of engine oil, the value of contact angles varied from ~ 6 to 25° indicating oleophilic nature (Figure 5a,b). The hydrophobicity and low density allowed the porous h-BN nanostructures to float on the water surface (inset Figure 5b). The study of contact angles of the samples heated for different durations revealed that hydrophobicity and oleophilicity changed as a function of porosity (Figure S6 in Supporting Information). Various types of the oils and organic solvents were demonstrated in the digital image along with the pellet samples having diameter of the order of $\sim 12.8\text{ mm}$ and thickness between 2 and 5 mm as shown in Figure 5b. The optimum oil absorption from water occurred in 15s (Figure S7 in Supporting Information). The different steps of the absorption process of engine oil have been illustrated (Figure S7 in Supporting Information) and further details can be found in Supporting Information. Demonstration for the used oils and organic solvents along with the pellets after

TABLE 1. Comparison of Synthesis Procedures, Density, and Compression Performance of the Synthesized Porous h-BN Solid with Other Porous Foams

synthesis route	density (mg/cm ³)	compressive stress (MPa)	ref
Solid state (porous h-BN solids)	890	83	Current work
Chemical route (Polyimide/graphene composite foam sheets)	~550	~44	37
Chemical route (syntactic foams reinforced with graphene platelets) (GP-SFs)	~920	~112	38
Unidirectional freeze-drying method (rGO foam with 2% GO)	~20	~0.005	39
Chemical route (rGO—CN)	~6.1	~0.006	40
Solution processing Method (GO-BN foams)	~5.0	~2.0	1
Chemical vapor deposition (CVD) (3-D graphene foam)	~ 5.0	~0.20	41

absorption were shown in Figure 5c. Figure 5d,e shows the uptakes of water, toluene, chloroform, engine oil, olive oil and mustard oil with values varying from 275 to 5680 wt %. It was reported that the porous BN nanosheets absorb up to 33 times their own weight of ethylene glycol and 29 times of used engine oil.³⁶ When the white pellets of the synthesized h-BN were dropped on the oil–water surface, they immediately absorbed the brown oil and became dark brown in color. This process was very fast as demonstrated in the Supporting Information (Figure S7). After 15 s, all oil was taken up by the porous h-BN pellet sample with a capacity of 5700 wt %. The saturated h-BN pellet sample still floated on the cleaned water surface and were therefore easy to be removed. More important is that the material is reusable several times by directly burning it in air to remove the absorbed organics from the porous h-BN material (Figure S8). Figure 5f shows the weight loss of porous h-BN in different concentrations of hydrochloric acid. It was observed that the

weight loss increased with increase in the concentration of the hydrochloric acid. The maximum weight loss is around 4 mg for 30 min soaking time. The comparison of the synthesis procedure, density, and compression performance of the porous h-BN solid with other porous foams is listed in Table 1.^{37–41}

CONCLUSION

In summary, nanostructured, ultra-low-density, and carbon-doped porous h-BN has successfully been synthesized using very simple solid state route. It exhibits excellent mechanical properties, with yield stress of 46.47–83.18 MPa. In addition, the porous h-BN exhibits excellent adsorption performance for oils as well as organic pollutants in water. Our simple and easily scalable synthesis method could pave the way for investigating the unique structure and properties of porous h-BN and exploiting its large number of potential applications including its net shape gain ability.

EXPERIMENTAL SECTION

Synthesis of h-BN. In a typical synthesis, 8.15 g of H₃BO₃ and 1.84 g of C₃N₆H₆ (molar ratio of 9:1) were mixed in acetone media for 6 h. Then, mixed powder was dried and transferred in to a porcelain crucible and kept in to a programmable electric furnace and sintered at 300 °C with heating rate of 5 °C/min for 3, 6, and 9 h soaking time. Eventually, white porous h-BN was produced. Pellets of the sintered powders were prepared using a load of 3 t for further measurements on it.

Material Characterization. X-ray diffraction (XRD) patterns of the samples were collected using a Rigaku D/Max Ultima II. The chemical composition was investigated by X-ray photoelectron spectroscopy (XPS, PHI Quantera XPS) on a PHI-5000C ESCA system with Al KR X-ray as an excitation source. Thermogravimetry (TG) and differential thermal analysis (DTA) were measured on a SDTQ-600 thermal analyzer from room temperature to 400 °C at a heating rate of 5 °C/min under nitrogen flow. The BET (Brunauer–Emmett–Teller) surface areas of the samples were measured using a Quantachrome Autosorb-3b BET Surface Analyzer. The morphology of the samples was observed using FEI Quanta 400 scanning electron microscope under high vacuum at 10 kV. A 10 nm thick gold film was sputtered on the sample before imaging to reduce the charging effect from h-BN sample. TEM images and diffraction patterns were taken using JEOL 2100 field emission gun transmission electron microscope. For preparing the TEM samples, tiny powder was taken and bath sonicated in isopropyl alcohol for 30 min. A few drops were then cast onto the holey carbon grids and allowed to dry in vacuum. The TEM samples were then left under vacuum overnight.

An advanced goniometer (500, Rame- Hart, Inc.) was used to measure the contact angle, θ° . A syringe was used to inject deionized water slowly onto the solid surface of the pellet samples. All the contact angle measurements were performed under equilibrium conditions. Q800 dynamic mechanical analysis was employed for performing mechanical test on the samples at room temperature and the values of the stiffness has been used to calculate the elastic modulus of the porous h-BN samples. Compressive stress versus strain curve was obtained from Instron universal testing machine.

Oil and Organic Solvent Absorption Capacity Measurements. The absorption capacity values, W (w/w)%, were obtained by measuring the mass of the h-BN samples, and then measuring the mass after oil/solvent absorption. The ratio of the final mass to the initial mass was taken as the W (w/w) value, averaging out three samples. To ensure complete saturation of the samples before weighing, they were left submerged in the solvent/oil (without water) overnight. The samples were then removed with sharp needle tweezers and immediately placed on weighing paper to measure their mass on the balance.

Simulations. For the density functional theory (DFT) calculations, we used the general gradient approximation (GGA-PBE) for the exchange-correlation functional^{42,43} as implemented in the OpenMX code. The core electrons were treated using norm-conserving pseudopotentials^{44–46} and the valence electrons wave functions expanded using pseudoatomic localized basis functions.⁴⁷ For the elements carbon (C), boron (B), and oxygen (O), three radial functions were considered to describe the s and p orbitals and two for the d orbital ($s^3p^3d^2$ basis set). For the

elements nitrogen (N) and hydrogen (H), $s^2p^3d^2f^1$ and s^2p^1 basis sets were considered, respectively. An energy cutoff of 250 Ry was considered for numerical integration and for the Poisson's equation solutions. The system was considered to be optimized when forces were below 5.0×10^{-4} Hartree/Bohr. For the molecular dynamic simulations, we considered a time step of 0.5 fs.

Conflict of Interest: The authors declare no competing financial interest.

Acknowledgment. The authors acknowledge the funding support from the U.S. Air Force Office of Scientific Research (Award No. FA9550-14-1-0268 and Award No. FA9550-12-1-0035). C. Gautam and S. Jose acknowledge financial support from University Grants Commission, New Delhi, Government of India, for the Raman Fellowship. G. Brunetto and D. S. Galvao acknowledge financial support from the Brazilian Agencies CNPq, CAPES, and FAPESP and thank the Center for Computational Engineering and Sciences at Unicamp for financial support through the FAPESP/CEPID Grant 2013/08293-7.

Supporting Information Available: The Supporting Information is available free of charge on the ACS Publications website at DOI: 10.1021/acsnano.5b05847.

Movie M1 (MPG)

XRD showing porous h-BN; XPS spectra of porous h-BN of samples; FTIR spectra of the samples; DTA and TGA curve of the initial mixture and processed samples; variation of percentage of porosity and surface area with soaking time of synthesized porous h-BN sintered at 300 °C for different soaking times, 3, 6, and 9 h, respectively; water and engine oil contact angles of porous h-BN synthesized at 300 °C; photograph of porous h-BN sample for the oil absorption test from water; photograph of burning oil-saturated porous h-BN in air for cleaning purpose (PDF)

REFERENCES AND NOTES

- Vinod, S.; Tiwary, C. S.; Autreto; Pedro, A. S.; Taha-Tijerina, J.; Ozden, S.; Chipara, A. C.; Vajtai, R.; Galvao, D. S.; Narayanan, T. N.; Ajayan, P. M. Low-density Three-Dimensional Foam Using Self-Reinforced Hybrid Two-Dimensional Atomic Layers. *Nat. Commun.* **2014**, *5*, 4541–4550.
- Chen, Z.; Ren, W.; Gao, L.; Liu, B.; Pei, S.; Cheng, H. M. Three-Dimensional Flexible and Conductive Interconnected Graphene Networks Grown by Chemical Vapour Deposition. *Nat. Mater.* **2011**, *10*, 424–428.
- Levdorf, M. P.; Kim, C. J.; Brown, L.; Huang, P. Y.; Havener, R. W.; Muller, D. A.; Park, J. Graphene and Boron Nitride Lateral Heterostructures for Atomically Thin Circuitry. *Nature* **2012**, *488*, 627–632.
- Ju, L.; Shi, Z.; Nair, N.; Lv, Y.; Jin, C.; V, J., Jr.; Ojeda-Aristizabal, C.; Bechtel, H. A.; Martin, M. C.; Zettl, A.; et al. Topological Valley Transport at Bilayer Graphene Domain Walls. *Nature* **2015**, *520*, 650–655.
- Tang, S.; Wang, H.; Wang, H. S.; Sun, Q.; Zhang, X.; Cong, C.; Xie, H.; Liu, X.; Zhou, X.; Huang, F.; et al. Silane-Catalyzed Fast Growth of Large Single-Crystalline Graphene on Hexagonal Boron Nitride. *Nat. Commun.* **2015**, *6*, 6499–6506.
- Sudeep, P. M.; Narayanan, T. N.; Ganesan, A.; Shajumon, M. M.; Yang, H.; Ozden, S.; Patra, P. K.; Pasquali, M.; Vajtai, R.; Ganguli, S.; et al. Covalently Interconnected Three-Dimensional Graphene Oxide Solids. *ACS Nano* **2013**, *7*, 7034–7040.
- Kotlensky, W. V.; Martens, H. E. Tensile Behavior of Pyrolytic Boron Nitride to 2200 °C. *Nature* **1962**, *196*, 1090–1091.
- Watanabe, K.; Taniguchi, T.; Kanda, H. Direct-Band Gap Properties and Evidence for Ultraviolet Lasing of Hexagonal Nitride Single Crystal. *Nat. Mater.* **2004**, *3*, 404–409.
- Jo, I.; Pettes, M. T.; Kim, J.; Watanabe, K.; Taniguchi, T.; Yao, Z.; Shi, L. Thermal Conductivity and Phonon Transport in Suspended Few-Layer Hexagonal Boron Nitride. *Nano Lett.* **2013**, *13*, 550–554.
- Siria, A.; Poncharal, P.; Biance, A. L.; Fulcrand, R.; Blase, X.; Purcell, S. T.; Bocquet, L. Giant Osmotic Energy Conversion Measured in a Single Transmembrane Boron Nitride Nanotube. *Nature* **2013**, *494*, 455–458.
- Golberg, D.; Bando, Y.; Huang, Y.; Terao, T.; Mitome, M.; Tang, C.; Zhi, C. Boron Nitride Nanotubes and Nanosheets. *ACS Nano* **2010**, *4* (6), 2979–2993.
- Pan, Y.; Huo, K. F.; Hu, Y. M.; Fu, J. J.; Lu, Y. N.; Dai, Z. D.; Hu, Z.; Chen, Y. Boron Nitride Nanocages Synthesized by a Moderate Thermochemical Approach. *Small* **2005**, *1*, 1199–1203.
- Yu, Y.; Chen, H.; Liu, Y.; Craig, V. S. J.; Wang, C.; Li, L. H.; Chen, Y. Superhydrophobic and Superoleophilic Porous Boron Nitride Nanosheet/Polyvinylidene Fluoride Composite Material for Oil-Polluted Water Cleanup. *Adv. Mater. Interfaces* **2015**, *2*, 1400267.
- Chen, L. Y.; Gu, Y. L.; Shi, L.; Yang, Z. H.; Ma, J. H.; Qian, Y. T. A Room-Temperature Approach to Boron Nitride Hollow Spheres. *Solid State Commun.* **2004**, *130*, 537–540.
- Liu, Z.; Gong, Y.; Zhou, W.; Ma, L.; Yu, J.; Idrobo, J. C.; Jung, J.; MacDonald, A. H.; Vajtai, R.; Lou, J.; et al. Ultrathin High-Temperature Oxidation-Resistant Coatings of Hexagonal Boron Nitride. *Nat. Commun.* **2013**, *4*, 2541–2549.
- Kalay, S.; Yilmaz, Z.; Sen, O.; Emanet, M.; Kazanc, E.; Culha, M. Synthesis of Boron Nitride Nanotubes and Their Applications. *Beilstein J. Nanotechnol.* **2015**, *6*, 84–102.
- Saner Okan, B.; Kocabas, Z. O.; Ergün, A. N.; Baysal, M.; Letofsky-Papst, I. L.; Yürüm, Y. Effect of Reaction Temperature and Catalyst Type on the Formation of Boron Nitride Nanotubes by Chemical Vapor Deposition and Measurement of Their Hydrogen Storage Capacity. *Ind. Eng. Chem. Res.* **2012**, *51*, 11341–11347.
- Liu, D.; Lei, W. W.; Qin, S.; Chen, Y. Template-Free Synthesis of Functional 3D BN Architecture for Removal of Dyes From Water. *Sci. Rep.* **2014**, *4*, 4453.
- Zhao, H.; Song, X.; Zeng, H. 3D White Graphene Foam Scavengers: Vesicant-Assisted Foaming Boosts the Gram-Level Yield and Forms Hierarchical Pores for Superstrong Pollutant Removal Applications. *NPG Asia Mater.* **2015**, *7*, e168.
- Zhang, C.; Zhao, S.; Jin, C.; Koh, A. L.; Zhou, Y.; Xu, W.; Li, Q.; Xiong, Q.; Peng, H.; Liu, Z. Direct Growth of Large-Area Graphene and Boron Nitride Heterostructures by a Co-Segregation Method. *Nat. Commun.* **2015**, *6*, 6519.
- Zhang, C.; Fu, L.; Zhao, S.; Zhou, Y.; Peng, H.; Liu, Z. Controllable Co-Segregation Synthesis of Wafer-Scale Hexagonal Boron Nitride Thin Films. *Adv. Mater.* **2014**, *26*, 1776–1781.
- Ci, L.; Song, L.; Jin, C.; Jariwala, D.; Wu, D.; Li, Y.; Srivastava, A.; Wang, Z. F.; Storr, K.; Balicas, L.; Liu, F.; Ajayan, P. M. Atomic Layers of Hybridized Boron Nitride and Graphene Domains. *Nat. Mater.* **2010**, *9*, 430–435.
- Tang, C.; Bando, Y.; Huang, Y.; Zhi, C.; Golberg, D. Synthetic Routes and Formation Mechanisms of Spherical Boron Nitride Nanoparticles. *Adv. Funct. Mater.* **2008**, *18*, 3653–3661.
- Zhi, C. Y.; Bando, Y.; Tang, C. C.; Golberg, D. Phonon Characteristics and Cathodoluminescence of Boron Nitride Nanotubes. *Appl. Phys. Lett.* **2005**, *86*, 213110–213113.
- Song, L.; Ci, L.; Lu, H.; Sorokin, P. B.; Jin, C.; Ni, J.; Kvashnin, A. G.; Kvashnin, D. G.; Lou, J.; Yakobson, B. I.; Ajayan, P. M. Large Scale Growth and Characterization of Atomic Hexagonal Boron Nitride Layers. *Nano Lett.* **2010**, *10*, 3209–3215.
- Hagio, T.; Kazuo, K.; Tadao, S. Formation of Hexagonal BN by Thermal Decomposition of Melamine Diborate. *J. Ceram. Soc. Jpn.* **1994**, *102*, 1051–1054.
- Devallencourt, C.; Saiter, J. M.; Fafet, A.; Ubrich, E. Thermo-gravimetry/Fourier Transform Infrared Coupling Investigations to Study the Thermal Stability of Melamine Formaldehyde Resin. *Thermochim. Acta* **1995**, *259*, 143–151.
- Liu, Y.; Wang, Y.; Zhou, S.; Lou, S.; Yuan, L.; Gao, T.; Wu, X.; Shi, X.; Wang, K. Synthesis of High Saturation Magnetization Superparamagnetic Fe_3O_4 Hollow Microspheres for

- Swift Chromium Removal. *ACS Appl. Mater. Interfaces* **2012**, *4*, 4913–4920.
29. Ma, R.; Bando, Y.; Sato, T. CVD Synthesis of Boron Nitride Nanotubes Without Metal Catalysts. *Chem. Phys. Lett.* **2001**, *337*, 61–64.
 30. Jin, C.; Lin, F.; Suenaga, K.; Iijima, S. Fabrication of a Freestanding Boron Nitride Single Layer and its Defect Assignments. *Phys. Rev. Lett.* **2009**, *102*, 195505.
 31. Deng, H.; Li, X.; Peng, Q.; Wang, X.; Chen, J.; Li, Y. Monodisperse Magnetic Single-Crystal Ferrite Microspheres. *Angew. Chem., Int. Ed.* **2005**, *44*, 2782–2785.
 32. Alem, N.; Emi, R.; Kisielowski, C.; Rossell, M. D.; Gannett, W.; Zettl, A. Atomically Thin Hexagonal Boron Nitride Probed by Ultrahigh-Resolution Transmission Electron Microscopy. *Phys. Rev. B: Condens. Matter Mater. Phys.* **2009**, *80*, 155425.
 33. Mannan, M. A.; Baba, Y.; Hirao, N.; Kida, T.; Nagano, M.; Noguchi, H. Hexagonal Nano-Crystalline BCN Films Grown on Si (100) Substrate Studied by X-Ray Absorption Spectroscopy. *Mater. Sci. Appl.* **2013**, *4*, 11–19.
 34. Rafiee, M. A.; Narayanan, T. N.; Hashim, D. P.; Sakhavand, N.; Shahsavari, R.; Vajtai, R.; Ajayan, P. M. Hexagonal Boron Nitride and Graphite Oxide Reinforced Multifunctional Porous Cement Composites. *Adv. Funct. Mater.* **2013**, *23*, 5624–5630.
 35. Pal, S.; Weiss, H.; Kellerb, H.; Müller-Plathez, F. The Hydrophobicity of Nanostructured Alkane and Perfluoro Alkane Surfaces: A Comparison by Molecular Dynamics Simulation. *Phys. Chem. Chem. Phys.* **2005**, *7*, 3191–3196.
 36. Li, J.; Xiao, X.; Xu, X.; Lin, J.; Huang, Y.; Xue, Y.; Jin, P.; Zou, J.; Tang, C. Activated Boron Nitride as an Effective Adsorbent for Metal Ions and Organic Pollutants. *Sci. Rep.* **2013**, *3*, 3208.
 37. Li, Y.; Pei, X.; Shen, B.; Zhai, W.; Zhang, L.; Zheng, W. Polyimide/Graphene Composite Foam Sheets with Ultra-high Thermostability for Electromagnetic Interference Shielding. *RSC Adv.* **2015**, *5*, 24342–24351.
 38. Zegeye, E.; Ghamsari, A. K.; Woldesenbet, E. Mechanical Properties of Graphene Platelets Reinforced Syntactic Foams. *Composites, Part B* **2014**, *60*, 268–273.
 39. He, Y.; Liub, Y.; Wub, T.; Ma, J.; Wang, X.; Gong, Q.; Kong, W.; Xing, F.; Liu, Y.; Gao, J. An Environmentally Friendly Method for the Fabrication of Reduced Graphene Oxide Foam with a Super Oil Absorption Capacity. *J. Hazard. Mater.* **2013**, *260*, 796–805.
 40. Barg, S.; Perez, F. M.; Ni, N.; Do Vale Pereira, P.; Maher, R. C.; Garcia-Tuñon, E.; Eslava, S.; Agnoli, S.; Mattevi, C.; Saiz, E. Mesoscale Assembly of Chemically Modified Graphene Into Complex Cellular Networks. *Nat. Commun.* **2014**, *5*, 4328.
 41. Nieto, A.; Dua, R.; Zhang, C.; Boesl, B.; Ramaswamy, S.; Agarwal, A. Three Dimensional Graphene Foam/Polymer Hybrid as a High Strength Biocompatible Scaffold. *Adv. Funct. Mater.* **2015**, *25*, 3916–3924.
 42. Hohenberg, P.; Kohn, W. Inhomogeneous electron Gas. *Phys. Rev.* **1964**, *136*, B864–B871.
 43. Perdew, J. P.; Burke, K.; Ernzerhof, M. Generalized Gradient Approximation Made Simple. *Phys. Rev. Lett.* **1996**, *77*, 3865–3868.
 44. Bachelet, G. B.; Hamann, D. R.; Schlüter, M. Pseudopotentials that Work: From H to Pu. *Phys. Rev. B: Condens. Matter Mater. Phys.* **1982**, *26*, 4199–4228.
 45. Troullier, N.; Martins, J. L. Efficient Pseudopotentials for Plane-Wave Calculations. *Phys. Rev. B: Condens. Matter Mater. Phys.* **1991**, *43*, 1993–2006.
 46. Morrison, I.; Bylander, D. M.; Kleinman, L. Nonlocal Hermitean Norm-Conserving Vanderbilt Pseudopotential. *Phys. Rev. B: Condens. Matter Mater. Phys.* **1993**, *47*, 6728–6731.
 47. Ozaki, T. Variationally Optimized Atomic Orbitals for Large-Scale Electronic Structures. *Phys. Rev. B: Condens. Matter Mater. Phys.* **2003**, *67*, 155108–155113.